Available online at www.sciencedirect.com
SCIENCE DIRECT®
Journal of Solid State Chemistry 176 (2003) 47–56
JOURNAL OF SOLID STATE CHEMISTRY
http://elsevier.com/locate/jssc

Stability and oxygen ionic conductivity of zircon-type $Ce_{1-x}A_xVO_{4+\delta}$ (A = Ca, Sr)

E.V. Tsipis,[a] V.V. Kharton,[a,b,*] N.P. Vyshatko,[a] A.L. Shaula,[a] and J.R. Frade[a]

[a] *Department of Ceramics and Glass Engineering, CICECO, University of Aveiro, 3810-193 Aveiro, Portugal*
[b] *Institute of Physicochemical Problems, Belarus State University, 14 Leningradskaya Str., 220050 Minsk, Belarus*

Received 30 December 2002; received in revised form 11 June 2003; accepted 12 June 2003

Abstract

Zircon-type $Ce_{1-x}A_xVO_{4+\delta}$ (A = Ca, Sr; $x = 0-0.2$) are stable in air up to approximately 1300 K, whilst further heating or reducing oxygen partial pressure leads to formation of A-site deficient zircon and $CeO_{2-\delta}$ phases. The stability boundaries of $Ce_{1-x}A_xVO_{4+\delta}$ are comparable to those of vanadium dioxide and calcium orthovanadate. At oxygen pressures lower than 10^{-15} atm, perovskite-type $CeVO_{3-\delta}$ is formed. The oxygen ion transference numbers of $Ce_{1-x}A_xVO_{4+\delta}$, determined by faradaic efficiency measurements in air, vary in the range from 2×10^{-4} to 6×10^{-3} at 973–1223 K, increasing with temperature. The oxygen ionic conductivity has activation energy of 87–112 kJ/mol and is essentially independent of A-site dopant content. Contrary to the ionic transport, p-type electronic conductivity and Seebeck coefficient of $Ce_{1-x}A_xVO_{4+\delta}$ are influenced by the divalent cation concentration. The average thermal expansion coefficients of $Ce_{1-x}A_xVO_{4+\delta}$, calculated from high-temperature XRD and dilatometric data in air, are $(4.7–6.1)\times10^{-6}\,K^{-1}$.

Keywords: Cerium vanadate; Zircon; Stability; Phase decomposition; Transference number; Faradaic efficiency; Conductivity; Seebeck coefficient; Thermal expansion

1. Introduction

Due to unique optical, electrical and redox properties, $CeVO_4$-based oxides are of considerable interest for numerous applications, such as counter electrodes in electrochromic devices, luminescent materials, gas sensors, oxidation catalysts and components of solid oxide fuel cell (SOFC) anodes [1–7]. Key properties determining applicability in the two latter cases include phase stability and the level of oxygen ionic and electronic conduction. The reduction of undoped zircon-type $CeVO_4$ was reported to proceed as a single-step transformation into $CeVO_3$ perovskite [4]. However, the conductivity of $CeVO_{3-\delta}$ exhibits a tendency to metallic behavior, which increases with acceptor-type doping [8], whereas $CeVO_4$ is a p-type semiconductor having activation energy for the electron–hole transport of about 36 kJ/mol [7,9]. This makes it possible to expect a greater conductivity when the zircon phase is transformed into perovskite. On the contrary, reducing oxygen partial pressure leads to a substantial decrease of the total conductivity, associated with phase decomposition [7]. Preliminary studies of the reduction products also showed that the decomposition mechanism is more complex than one-step conversion [7].

Crystal structure of the zircon-type polymorph of $CeVO_4$, stable at atmospheric pressure, is tetragonal with space group $I4_1/amd$ [10,11]; most cerium cations exist in trivalent state even in air [9,12]. Although a transition into scheelite modification was assumed at temperatures above 1100 K [13], this transformation was not confirmed experimentally. Substitution of cerium with divalent metal cations, such as Ca and Sr, leads to zircon lattice contraction and increasing total conductivity due to the formation of electron–holes located on cerium ions [7,9]. The maximum conductivity in air was found for the compositions $Ce_{0.8}Ca_{0.2}VO_4$ and $Ce_{0.9}Sr_{0.1}VO_4$ [9]. In addition, doping with calcium enhances phase stability of cerium orthovanadate,

*Corresponding author. Present address: Department of Ceramics and Glass Engineering, CICECO, University of Aveiro, 3810-193 Aveiro, Portugal. Fax: +351-234-370263.
E-mail address: kharton@cv.ua.pt (V.V. Kharton).

0022-4596/$ - see front matter © 2003 Elsevier Inc. All rights reserved.
doi:10.1016/S0022-4596(03)00342-6

Table 1
Properties of $Ce_{1-x}A_xVO_4$ ceramics

Composition	Unit cell parameters		Specific free volume	d_{exp}/d_{theor} (%)	Activation energy (kJ/mol)	
	a (Å)	c (Å)			Ionic transport	Electron–hole transport
$CeVO_4$	7.398(7)	6.498(2)	0.542	99	112±14	45±7
$Ce_{0.9}Ca_{0.1}VO_4$	7.354(0)	6.472(0)	0.517	93	93±8	42±3
$Ce_{0.8}Ca_{0.2}VO_4$	7.335(3)	6.460(8)	0.512	97	91±9	40±7
$Ce_{0.9}Sr_{0.1}VO_4$	7.381(0)	6.491(5)	0.519	95	87±7	39±1

Note: d_{exp}/d_{theor} is the ratio between experimental and theoretical density.

evaluated from the data on conductivity and Seebeck coefficient as functions of the oxygen partial pressure [7].

The results on structure and electrical properties of Ca-doped $CeVO_4$ suggest a moderate oxygen excess in the lattice, leading to an interstitial mechanism of the oxygen ion diffusion [7]. This is typical for other $Ce^{III}B^{V}O_{4+\delta}$ compounds, where B is pentavalent cation such as Ta^{5+} [14]. In $Ce(Ca)VO_{4+\delta}$ the hyperstoichiometry is rather low, less than 2–3% of the total oxygen content [7]; the experimental data of X-ray-absorption spectroscopy [12] and thermogravimetric analysis [9] cannot rule out presence of minor fraction of Ce^{4+}. Notice also that oxygen ion migration in the interstitial sites along the c-axis of the zircon lattice is known for other rare-earth orthovanadates, such as $EuVO_4$ [15].

The present work is in continuation to our studies of cerium oxide-based materials [7,16–20] and is focused on oxygen ionic conduction and zircon phase decomposition in $Ce_{1-x}A_xVO_{4+\delta}$ (A = Ca, Sr; $x = 0-0.2$). The stability boundaries of $Ce_{1-x}Ca_xVO_{4+\delta}$, estimated from total conductivity and Seebeck coefficient measurements [7], are verified using X-ray diffraction (XRD) data. High-temperature XRD is also used to study thermal expansion, another factor important for the electrochemical and catalytic applications.

2. Experimental

Single-phase powders of $CeVO_4$, $Ce_{0.9}Sr_{0.1}VO_4$, $Ce_{0.9}Ca_{0.1}VO_4$ and $Ce_{0.8}Ca_{0.2}VO_4$ were synthesized by a standard ceramic technique from high-purity $Ce(NO_3)_3 \cdot 6H_2O$ (Aldrich), V_2O_5 (Fluka), $SrCO_3$ (BDH) and $CaCO_3$ (Fluka) as starting materials. The solid-state reactions were conducted at 820–1120 K for 10–30 h in air using closed alumina crucibles. The synthesis procedure consisted of 4–7 steps, which included annealing for 3–5 h, regrinding and X-ray diffraction (XRD) analysis. These steps were repeated with a gradual increase of annealing temperature, until XRD showed formation of single zircon-type phases. The synthesized powders were ball-milled for 4 h and compacted at 200–350 MPa into disks (diameter 15 mm). Gas-tight ceramics were sintered at 1470–1650 K, during 5 h, with subsequent slow cooling, in order to achieve equilibrium with air. The density of ceramic materials was 93–99% of their theoretical density (Table 1).

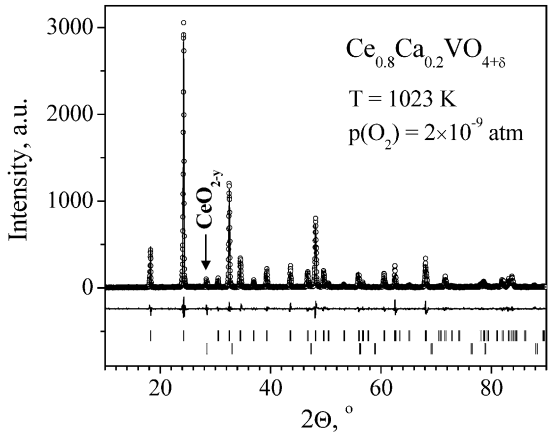

Fig. 1. Observed, calculated and difference XRD pattern of CeO_{2-y} containing $Ce_{0.8}Ca_{0.2}VO_{4+\delta}$ ceramics at 1023 K in vacuum.

Room temperature XRD patterns were recorded using a Rigaku D/Max-B diffractometer; a Philips X'Pert MPD apparatus was used for the high-temperature XRD studies. In both cases the scans were performed in the 2θ range from 10° to 100° (Cu$K\alpha$ radiation, step 0.02°, 2 s/step). Room temperature XRD was used for either equilibrated samples or for the materials quenched from 923 to 1373 K in liquid nitrogen. Before quenching, porous ceramic samples were annealed at a fixed temperature in flowing air, argon or 10%H_2–90%N_2 mixture for 2–50 h; the oxygen partial pressure was independently measured by an oxygen sensor. High-temperature XRD studies were carried out at 300–1223 K in air and in vacuum (oxygen partial pressure of approximately 2×10^{-9} atm). Structure refinement was made using the Fullprof program [21]. In the case of partial decomposition resulting in separation of cerium oxide, structural parameters of the major zircon-type phase were refined on the first step; then the secondary phase, CeO_{2-y}, was included in the refinement. Fig. 1 presents an example of the two-phase mixture refinement results.

The ceramic materials were characterized by scanning electron microscopy combined with energy dispersive spectroscopy (SEM/EDS), ion-coupled plasma (ICP)

emission spectroscopic analysis, dilatometry and impedance spectroscopy; experimental procedures and equipment were reported elsewhere [16–20]. Thermal expansion measurements were carried out in air using an alumina Linseis dilatometer (heating rate of 5 K/min). At temperatures above 900 K, dilatometric curves showed an anomalous behavior, which was associated with a very poor reproducibility and resulted, most probably, from chemical interaction between Ce(A)VO_4 ceramics and alumina, visible after experiments; the maximum temperature used in the course of dilatometric studies was therefore limited to 853 K. The total conductivity (σ) and Seebeck coefficient (α) were measured in the temperature range 323–1223 K at oxygen partial pressures from 6×10^{-26} to 0.75 atm, as described earlier [7,22]. The oxygen ion transference numbers (t_o) were determined at 973–1223 K by the faradaic efficiency technique [17]; the measurements were carried out under zero oxygen chemical potential gradient in air. Each t_o value was averaged from 2–4 experimental points. The values of oxygen ionic (σ_o) and p-type electronic (σ_p) conductivities were calculated from the results of total conductivity and faradaic efficiency measurements.

3. Results and discussion

3.1. Thermal expansion and ceramic microstructure

XRD studies showed that both synthesized powders and sintered ceramics of $Ce_{1-x}A_xVO_{4+\delta}$ were single-phase; the parameters of the tetragonal zircon-type unit cells are listed in Table 1. When cerium is substituted with alkaline-earth cations, the unit cell parameters decrease, in agreement with literature data [9,23]. This behavior suggests a charge compensation mechanism via formation of tetravalent cerium cations. The radii of Ca^{2+} and Ce^{3+} ions are similar, both smaller than that of Sr^{2+}; 8-coordinated Ce^{4+} has a substantially smaller size than Ce^{3+} [24]. The lattice contraction is therefore attributed to forming Ce^{4+} cations, which was confirmed by the Seebeck coefficient and total conductivity results [7].

The temperature dependencies of the unit cell parameters calculated from high-temperature XRD data are linear within the temperature range of 300–1223 K (Fig. 2). The thermal expansion has a significantly anisotropic character, being greater for c-axis than for a. The linear thermal expansion coefficients (TECs) are $(2.8–3.1)\times10^{-6}$ and $(6.8–10.2)\times10^{-6}\,K^{-1}$ for the a and c parameters, respectively (Table 2). This corresponds to the average linear TECs (α_L), which can be estimated from the volume thermal expansion coefficients (β) as $\alpha_L=\beta/3$, to vary in the range $(4.3–5.4)\times10^{-6}\,K^{-1}$.

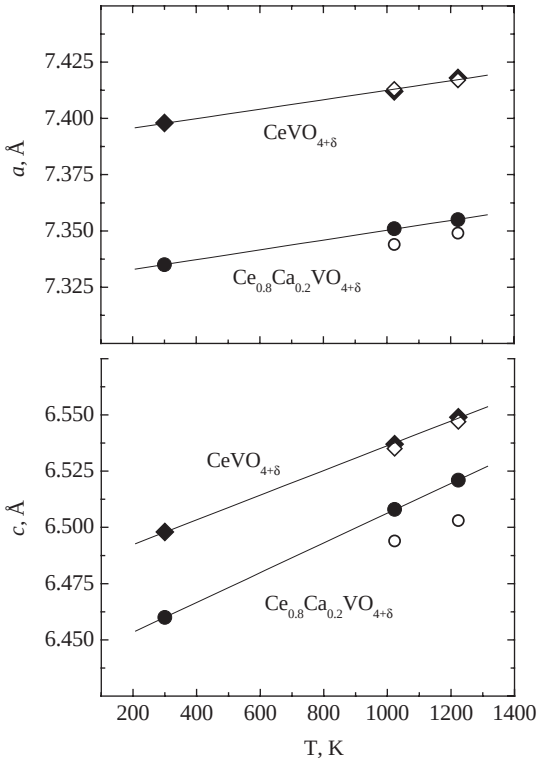

Fig. 2. Temperature dependencies of the tetragonal unit cell parameters of zircon-type $CeVO_{4+\delta}$ and $Ce_{0.8}Ca_{0.2}VO_{4+\delta}$ in air (closed symbols) and in vacuum (open symbols).

Table 2
Linear thermal expansion coefficients of $CeVO_4$ and $Ce_{0.8}Ca_{0.2}VO_4$, calculated from high-temperature XRD and dilatometric data

Composition	$p(O_2)$, atm	XRD				Dilatometry	
		T (K)	$\alpha_a\times10^6$ (K^{-1})	$\alpha_c\times10^6$ (K^{-1})	$\alpha_L\times10^6$ (K^{-1})	T (K)	$\bar{\alpha}\times10^6$ (K^{-1})
$CeVO_4$	0.21	300–1123	2.8	8.5	4.7	390–853	5.65
	2×10^{-9}	1023–1223	2.3	9.2	4.6	—	—
$Ce_{0.8}Ca_{0.2}VO_4$	0.21	300–1123	2.9	10.2	5.4	390–853	5.64
	2×10^{-9}	1023–1223	3.1	6.8	4.3	—	—

Notes: α_a and α_c are the TEC values for the a and c axes of zircon lattice, respectively; α_L is the average linear TEC, related to the volume thermal expansion coefficient (β) as $\alpha_L=\beta/3$.

The dilatometric curves of $Ce_{1-x}A_xVO_{4+\delta}$ ceramics are also linear (Fig. 3). The TEC values, calculated from dilatometric data in air, vary in the narrow range $(5.6–6.1)\times10^{-6}\,K^{-1}$ at 390–853 K and are very similar to the high-temperature XRD results. Note that the dilatometric TECs of $Ce_{0.9}A_{0.1}VO_{4+\delta}$ compounds, $5.85\times10^{-6}\,K^{-1}$ for $A=Ca$ and $6.09\times10^{-6}\,K^{-1}$ for $A=Sr$, were slightly higher than for two other compositions.

Typical SEM micrographs of $Ce(A)VO_{4+\delta}$ ceramics are presented in Fig. 4. The grains of the dense ceramic materials are rather large, having an average size from 5 to 25 μm. Some traces of a liquid phase possibly assisted the sintering process were observed at the grain boundaries. However, the impedance spectra exhibit only a single arc, even at temperatures as low as 300–400 K (Fig. 5). The capacity associated with this arc was less than $(6–7)\times10^{-11}$ F/cm, which can be definitely attributed to the bulk process. No grain boundary contribution to the total resistivity was also detected at low oxygen partial pressures, as illustrated by the inset in Fig. 5. In addition, it should be separately mentioned that the impedance spectroscopy showed no electrode effects, in agreement with very low values of the oxygen ion transference numbers of $Ce_{1-x}A_xVO_{4+\delta}$, discussed below.

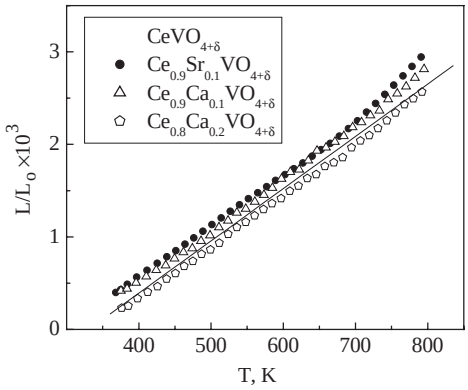

Fig. 3. Dilatometric curves of $Ce(A)VO_{4+\delta}$ ceramics in air.

3.2. Evaluation of phase relationships

In atmospheric air, zircon-type phases $Ce(A)VO_{4+\delta}$ were found stable up to, at least, 1300 K. The high-temperature XRD data and the analysis of samples quenched in liquid nitrogen proved no phase changes. Increasing temperature to 1373 K results in the formation of two phases, CeO_2 and the corresponding A-site deficient zircon $Ce_{1-x}VO_{4\pm\delta}$. The content of CeO_{2-y} at 1373 K in air was observed to be as high as 30%; an example of the XRD pattern is given in Fig. 6. This seems quite contrary to the assumption [13] concerning a transformation of the zircon- to scheelite-type phase of $CeVO_4$ around 1173 K, suggested to explain the unusual

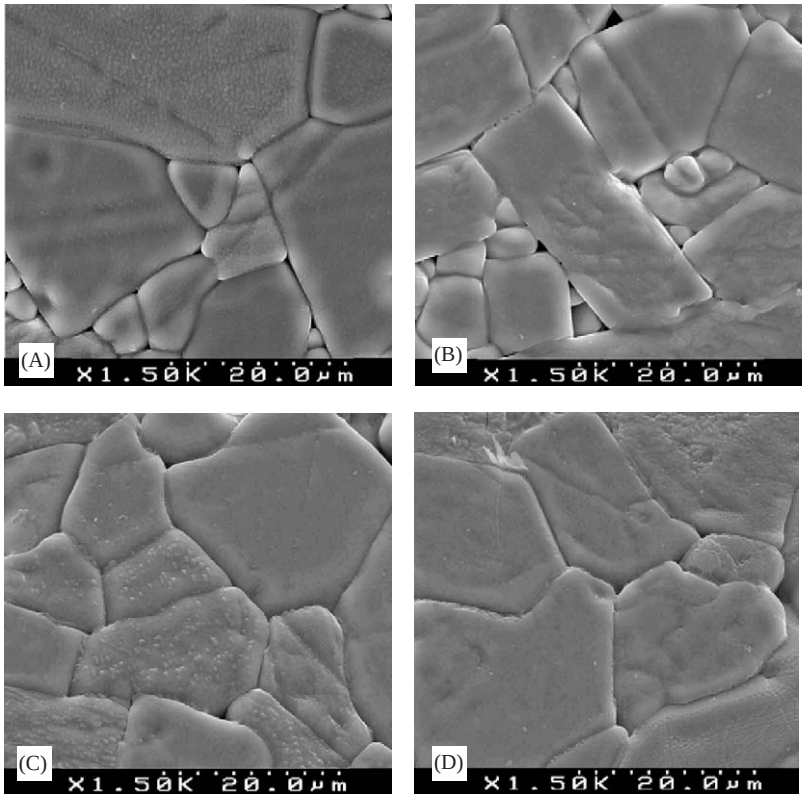

Fig. 4. SEM micrographs of $CeVO_4$ (A), $Ce_{0.9}Sr_{0.1}VO_4$ (B), $Ce_{0.9}Ca_{0.1}VO_4$ (C), and $Ce_{0.8}Ca_{0.2}VO_4$ (D) ceramics.

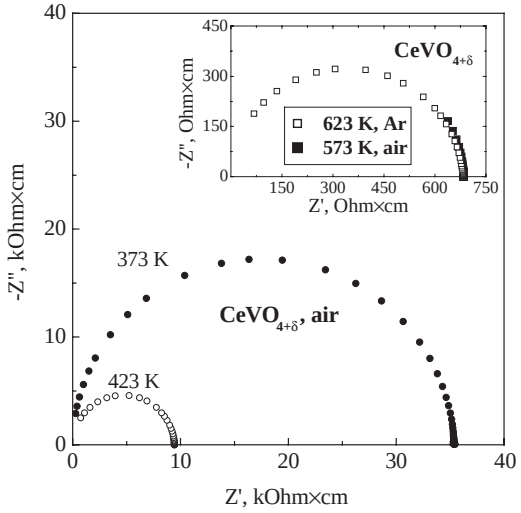

Fig. 5. Examples of the impedance spectra of $CeVO_{4+\delta}$ ceramics, collected at 423–573 K in air and in argon.

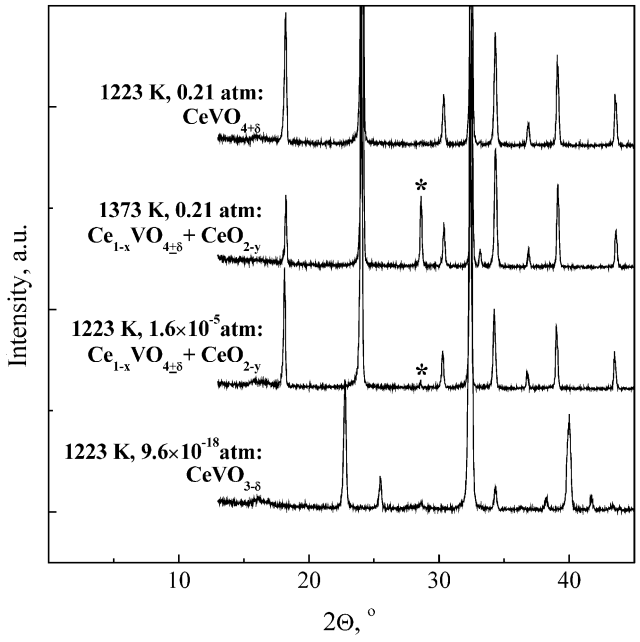

Fig. 6. Examples of XRD patterns of $CeVO_{4+\delta}$ quenched after annealing in various atmospheres, illustrating phase relationships discussed in the text. The strongest reflection of CeO_{2-y} is marked by asterisk.

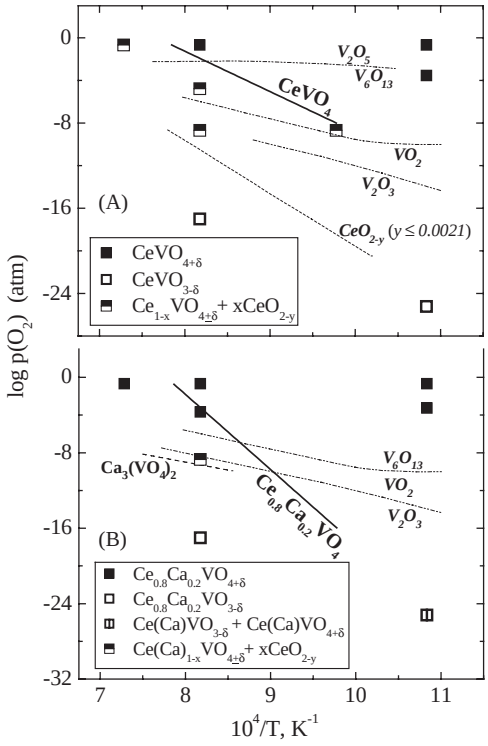

Fig. 7. Selected results of XRD analysis and phase stability limits of $CeVO_{4+\delta}$ (A) and $Ce_{0.8}Ca_{0.2}VO_{4+\delta}$ (B). Solid lines correspond to the phase boundaries estimated from the data on conductivity and Seebeck coefficient. Dashed lines correspond to the stability limits of $Ca_3(VO_4)_2$ [27] and binary vanadium oxides [28]. Oxygen isoconcentration line in $CeO_{1.9979}$ [29] is shown for comparison.

conductivity behavior and the results of differential thermal analysis (DTA). The difference in behavior could be ascribed, in particular, to different preparation routes used in this work and in Ref. [13]. Also, the phenomena observed by the authors [13] may be caused by CeO_2 separation.

Although the thermal expansion coefficients in vacuum are quite similar to those in air (Table 2), reducing oxygen partial pressure down to 2×10^{-9} atm also leads to segregation of oxygen-deficient CeO_{2-y} and, thus, to the unit cell contraction (Fig. 2). In vacuum, the amount of segregated cerium oxide at 1023–1223 K, estimated from the structure refinement results, was 3–5 mol% in the case of $CeVO_4$ and up to 8–12 mol% for $Ce_{0.8}Ca_{0.2}VO_4$; one example is shown in Fig. 1. Similar behavior is observed for $CeVO_4$ samples annealed in a flow of argon, where $p(O_2)=10^{-5}$ atm, at 1223 K (Fig. 6). For $Ce_{0.8}Ca_{0.2}VO_4$, no traces of zircon phase decomposition after annealing in argon were found (Fig. 7).

Further reduction of the oxygen partial pressure results in a transition of the zircon-type phases into $CeVO_3$-based perovskites (Fig. 6), in agreement with thermodynamic data [25]. This transformation occurred for all samples annealed in a flow of 10% H_2–90% N_2 mixture at 973–1223 K. At 923 K, the conversion of $Ce_{0.8}Ca_{0.2}VO_4$ into $Ce(Ca)VO_{3-\delta}$ perovskite was incomplete; only about 7 mol% of perovskite phase was formed after the reduction. However, such a behavior can be ascribed, most likely, to kinetic limitations.

Selected results on the phase relations in Ce(Ca)-$VO_{4\pm\delta}$ systems, evaluated from the XRD data at different temperatures and oxygen partial pressures, are summarized in Fig. 7. The solid lines correspond to

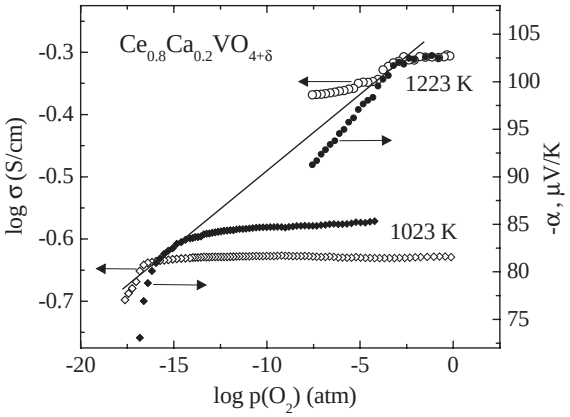

Fig. 8. Oxygen partial pressure dependence of the total conductivity and Seebeck coefficient of $Ce_{0.8}Ca_{0.2}VO_{4+\delta}$, illustrating evaluation of the phase stability boundary shown as solid line.

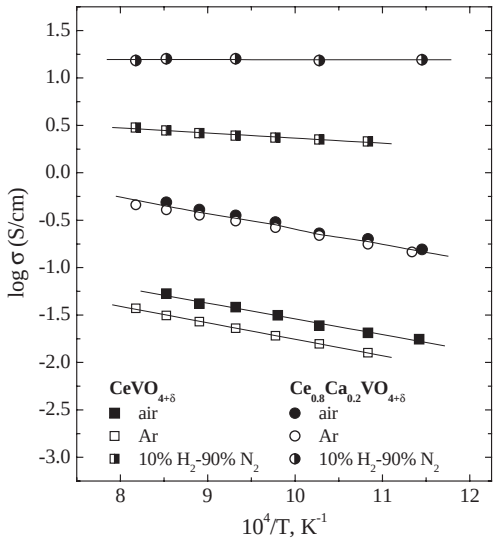

Fig. 9. Temperature dependence of the total conductivity of $CeVO_{4+\delta}$ and $Ce_{0.8}Ca_{0.2}VO_{4+\delta}$ ceramics in various atmospheres.

the stability boundaries estimated from $p(O_2)$-dependencies of the total conductivity and Seebeck coefficient, as shown in Fig. 8. Detailed data on the electrical properties as functions of the oxygen pressure are found elsewhere [7]. The XRD results are in a good agreement with the phase boundary estimates. This means that a sharp decrease in the conductivity curves and the corresponding increase of Seebeck coefficient result from starting of cerium oxide segregation due to the decomposition process. The conductivity of CeO_{2-y} [26] is considerably lower than that of $CeVO_4$-based phases [7,9]. The volume fraction of segregated cerium oxide is small but it may still affect the conductivity by preferential segregation at grain boundaries. Notice also that, in most cases, the changes in conductivity and Seebeck coefficient of $Ce_{1-x}A_xVO_{4+\delta}$ at reduced oxygen partial pressures were irreversible.

In order to verify phase relationships assessed by XRD analysis, the temperature dependencies of total conductivity were studied in different atmospheres (Fig. 9). For $Ce_{0.8}Ca_{0.2}VO_{4+\delta}$ ceramics which are single-phase both in air and in argon, the change in the oxygen partial pressure from 0.21 to 1×10^{-5} atm results in a slight decrease of the σ values. On the contrary, the conductivity of undoped $CeVO_{4+\delta}$ in air is considerably higher than that in argon where the segregation of ceria is observed. When both compositions are converted into the perovskite phases in hydrogen atmosphere, the values of σ increase 10–80 times, in agreement with literature on perovskite-type vanadates [8]. The total conductivity of $Ce_{0.8}Ca_{0.2}VO_{3-\delta}$ shows a metallic behavior, being essentially independent of temperature.

3.3. Zircon phase decomposition

The XRD and conductivity data show that, at low oxygen pressures and temperatures above 1000 K, CeO_{2-y} segregates from the zircon-type phases; further reduction results in a conversion of the two-phase mixtures into perovskite phase. Therefore, the reduction mechanism of $Ce(Ca)VO_{4\pm\delta}$ at $T>1000$ K is more complex than one-step transformation "zircon→perovskite", suggested in Ref. [4] for temperatures about 900 K. This mechanism should include at least two stages, which may be expressed as

$$CeVO_{4+\delta1} \rightarrow Ce_{1-x}VO_{4\pm\delta2} + xCeO_{2-y} + 1/2(\delta_1 \mp \delta_2 - 2x + xy)O_2, \quad (1)$$

$$Ce_{1-x}VO_{4+\delta2} + xCeO_{2-y} \rightarrow CeVO_{3-\delta3} + 1/2(\delta_1 \pm \delta_2 + \delta_3 - 2x - xy)O_2, \quad (2)$$

where δ_1 and δ_2 are the oxygen nonstoichiometry values of the cation-stoichiometric and A-site-deficient zircon phases, and δ_3 is the nonstoichiometry of perovskite. The latter phase is presumably oxygen-deficient, especially when significant amounts of the acceptor-type dopants are incorporated in the lattice. The mechanism expressed by Eqs. (1) and (2) implies that the amount of segregated CeO_{2-y} should increase with decreasing oxygen partial pressure until the perovskite phase is separated; then reducing oxygen chemical potential should lead to disappearing of cerium oxide phase, in agreement with experimental data.

Fig. 7 compares the stability boundaries of $Ce(Ca)VO_{4+\delta}$ with thermodynamic data on calcium vanadate [27] and binary oxides of vanadium and cerium [28,29]. In the case of vanadium oxides, dashed lines in Fig. 7 correspond to the phase boundaries between different V–O phases [28]; for oxygen-deficient CeO_{2-y} [29] the dashed line relates to the fixed nonstoichiometry value, $y=0.0021$. The first step of $Ce(Ca)VO_{4+\delta}$ reduction is close to the oxygen partial pressures of $V_6O_{13}\rightarrow VO_2\rightarrow$

V_2O_3 transitions and can thus be associated with reducing of vanadium cations. The zircon-type lattice is expected to stabilize V^{5+} oxidation state, as for $Ca_3(VO_4)_2$ where decomposition takes place at $p(O_2)$ values close to VO_2 phase boundary. Further conversion into $Ce(Ca)VO_{3-\delta}$ perovskite is related to the formation of Ce^{3+} and V^{3+} cations; the onset of the perovskite phase is observed mainly for conditions when both single oxides are reduced to the trivalent state.

Substitution of cerium with calcium leads to increasing oxidation state of vanadium cations at reduced oxygen pressures, thus enhancing stability of zircon phase (Fig. 7). In fact, the stability boundary of $Ce_{0.8}Ca_{0.2}VO_4$ at temperatures above 1100 K is intermediate between those of $CeVO_4$ and $Ca_3(VO_4)_2$. At the same time, Ca doping seems to affect phase decomposition mechanism. As mentioned above, the amount of cerium oxide, segregated from $Ce_{0.8}Ca_{0.2}VO_4$ at 1023–1223 K and $p(O_2)=2\times10^{-9}$ atm, was considerably higher than that for $CeVO_4$. This might suggest that decomposition of Ca-substituted phase occurs via formation of $Ce(Ca)O_{2-\delta}$ solid solution, which may promote zircon decomposition; further studies are necessary to identify exact mechanism responsible for this behavior.

Perovskite-type $Ce(Ca)VO_{3-\delta}$ exhibits better transport properties than the zircon-type compounds, but its stability with respect to re-oxidizing is poor. Nevertheless, divalent additives may stabilize the perovskite phase by allowing partial re-oxidation of cerium and/or vanadium to higher valence states. From the point of view of the tolerance factor of perovskite structure, one should expect an enhanced stability by allowing partial oxidation from V^{3+} to V^{4+}. On the contrary, oxidation of Ce^{3+} to Ce^{4+} should lower the stability.

3.4. Oxygen ionic and p-type electronic conduction

Fig. 10 presents the oxygen ion transference numbers of $Ce_{1-x}A_xVO_{4+\delta}$ (A=Ca, Sr; $x=0-0.2$) ceramics, determined by the faradaic efficiency measurements in air. The ion transference numbers vary in the range from 2×10^{-4} to 6×10^{-3} at 973–1223 K and increase with temperature. Increasing concentration of alkaline-earth cations leads to decreasing ionic contribution to the total conductivity.

The Arrhenius plots of partial oxygen-ionic and p-type electronic conductivities are shown in Figs. 11 and 12; the corresponding activation energies are listed in Table 1. Possible mechanisms of electron–hole transport were analyzed earlier [7]; in this paper one can briefly note that incorporation of alkaline-earth cations in the zircon-type lattice results in increasing p-type conduction and decreasing Seebeck coefficient due to formation of electron–holes localized on cerium ions. Respectively, hole conductivity and thermopower both are determined

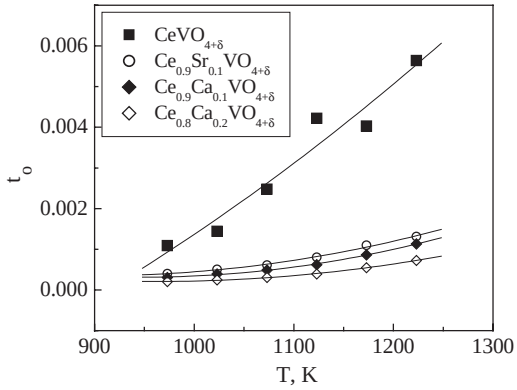

Fig. 10. Temperature dependencies of the oxygen ion transference numbers of $Ce_{1-x}A_xVO_{4+\delta}$, determined by the faradaic efficiency measurements in air.

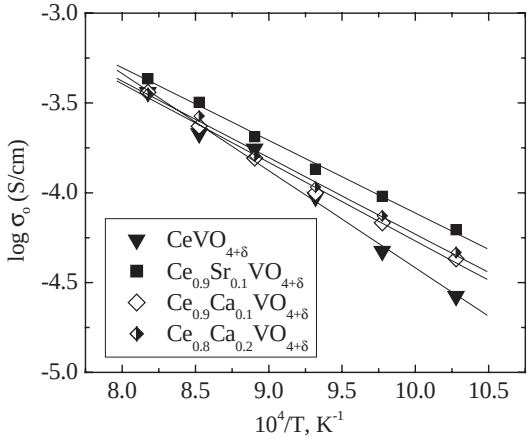

Fig. 11. Temperature dependence of the oxygen ionic conductivity of $Ce_{1-x}A_xVO_{4+\delta}$ ceramics in air.

by the A^{2+} cation concentration, being essentially independent of the dopant type (Fig. 12).

Contrary to the p-type electronic transport, the oxygen ionic conduction weakly depends on the alkaline-earth dopant content (Fig. 11). For instance, σ_o values of $Ce_{1-x}Ca_xVO_{4+\delta}$ with $x=0.1$ and 0.2 are almost equal, within the limits of experimental error. The similar values of the ionic conductivity in $Ce(Ca)VO_{4+\delta}$ result from the interstitial ion migration mechanism [7]. Indeed, if cerium vanadate would be nearly stoichiometric with the prevailing charge compensation mechanism via the oxygen vacancy formation [9,23], a systematic increase in the ionic conductivity should be expected due to increasing vacancy concentration when calcium content increases. One typical example of such behavior refers to acceptor-doped perovskites and fluorites, such as $(La,Sr)CoO_{3-\delta}$ or $Ce(A)O_{2-\delta}$ [26,30], where incorporation of moderate amounts of lower-valence cations leads to increasing

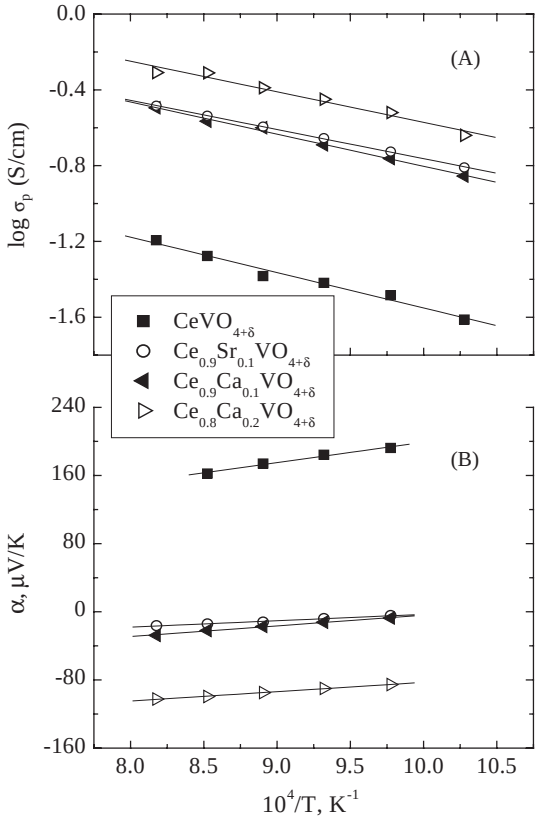

Fig. 12. Temperature dependence of the partial *p*-type electronic conductivity (A) and Seebeck coefficient (B) of $Ce_{1-x}A_xVO_{4+\delta}$ ceramics in air.

ionic conduction, almost proportional to the induced oxygen nonstoichiometry. Therefore, the observed behavior (Fig. 11) should be rather attributed to predominant interstitial diffusion due to the presence of hyperstoichiometric oxygen in the lattice, with negligible vacancy contribution. Calcium charge compensation occurs mainly via formation of electron–holes located on Ce cations, which has no essential effect on the anion charge carrier concentration. At 973–1073 K the ionic conductivity of undoped cerium vanadate is slightly lower, but becomes similar to that in Ce(Ca)-$VO_{4+\delta}$ at temperatures above 1100 K. Such a behavior could be attributed to the oxygen uptake on heating, characteristic of $CeVO_{4+\delta}$ in air [7].

The oxygen ionic conductivity of Sr-doped vanadate was found to be slightly higher with respect to Ca-containing compositions (Fig. 11). Therewith, $Ce_{0.9}Sr_{0.1}VO_{4+\delta}$ and $Ce_{0.9}Ca_{0.1}VO_{4+\delta}$ possess essentially the same values of Seebeck coefficient and, thus, electron–hole concentration (Fig. 12B). As the latter is directly proportional to the oxygen hyperstoichiometry according to the crystal electroneutrality law, the concentrations of the ionic charge carriers in $Ce_{0.9}Sr_{0.1}VO_{4+\delta}$ and $Ce_{0.9}Ca_{0.1}VO_{4+\delta}$ are expected to be very similar; the higher ionic conduction in Sr-containing compound is hence related to a greater oxygen-ion mobility.

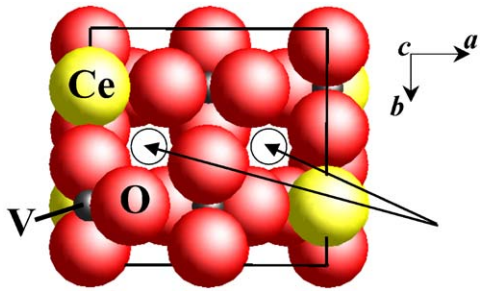

Fig. 13. Projection of zircon-type lattice of $CeVO_{4+\delta}$, drawn using structure refinement results and ionic radii from Ref. [24]. Square and circles show the unit cell and the most probable channel for the interstitial oxygen transport along *c*-axis, respectively.

Analogous tendencies in ABO_3 perovskite oxides, where increasing *A*-site cation radius leads to increasing ionic transport [30,31], can be explained in terms of various geometrical parameters, including the size of ion migration channels and free volume of the lattice [32,33]. In the case of zircon structure, however, these concepts seem rather invalid. As an example, Fig. 13 shows a projection of $CeVO_4$ unit cell, drawn on the basis of structure refinement results and ionic radii from Ref. [24], in the direction perpendicular to *c*-axis; the probable migration channels of oxygen interstitials in zircon-type lattice [7,15] are marked by circles. For $Ce_{1-x}A_xVO_{4+\delta}$ the size of these channels (so-called "bottlenecks") is 30–40% smaller than the diameter of oxygen ion. Respectively, no correlation between the bottleneck size and ionic conductivity was found, as expected from this comparison. The specific free volume of the lattice of $Ce_{1-x}A_xVO_{4+\delta}$ (Table 1) is defined as $(V-V_{ion})/V$, where V is the unit cell volume and V_{ion} is the volume of ions constituting the cell [33]. Again, no correlation of the free volume with ionic conduction is observed, suggesting that the concept of free volume developed for perovskites cannot be applied for the zircon structure. The ideal perovskite lattice presents a three-dimensional network of equivalent diffusion pathways, where the jump probability is equal for all oxygen ions; the specific free volume reflects, therefore, volume of each migration channel. This is not valid in the case of zircon, where only a minor part of oxygen ions may contribute to ionic conduction and the transport is one-dimensional (Fig. 13).

The higher ionic conductivity of $Ce_{0.9}Sr_{0.1}VO_{4+\delta}$ with respect to other vanadates may hence be explained in terms of hypothesis [30], regarding possible influence of *A*-site cation polarizability on the anion mobility, or assuming a strong cooperative effect in the processes of ion migration. The assumption [30] refers to increasing polarizability of *A*-site cations with similar charge when the average cation radius increases; this is expected to

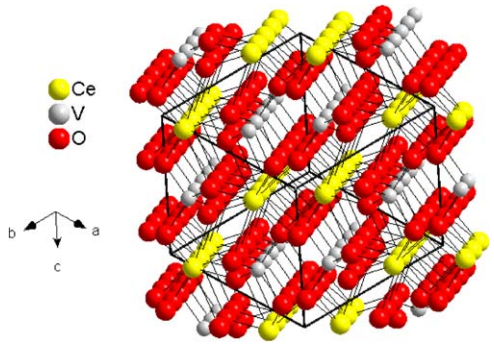

Fig. 14. Fragment of zircon-type structure of $Ce_{1-x}A_xVO_4$, showing the oxygen chains along [1,1,−1] direction.

decrease cation–anion interaction and, thus, potential barrier for ion jumps. Such effect may explain variations of the oxygen ionic transport in a number of perovskite- and K_2NiF_4-type mixed conductors [30,31]. One alternative hypothesis relates to a significant contribution of the oxygen jumps along [1,1,−1] direction as illustrated by Fig. 14; oxygen vacancies in these oxygen chains can be formed due to a Frenkel-type disorder. In this case, again, the size and polarizability of *A*-site cations is expected to play an important role.

4. Conclusions

Zircon-type $Ce_{1-x}A_xVO_{4+\delta}$ (A = Ca, Sr; $x = 0-0.2$) are stable at atmospheric oxygen pressure up to approximately 1300 K, whilst decreasing $p(O_2)$ or further heating in air leads to the formation of *A*-site deficient zircon and $CeO_{2-\delta}$ phases. In reducing atmospheres where $p(O_2)$ is lower than 10^{-15} atm, perovskite-like $Ce(A)VO_{3-\delta}$ are formed. The stability limits of zircon-type compounds at 1000–1300 K are comparable to the boundaries between binary vanadium oxides, V_6O_{13}–VO_2–V_2O_3. The average TECs of $Ce_{1-x}A_xVO_{4+\delta}$, calculated from the high-temperature XRD and dilatometric data in air, are quite similar and vary in the range $(4.7–6.1)\times10^{-6}\,K^{-1}$. The zircon lattice exhibits a significant anisotropy of thermal expansion, which is significantly higher for *c*-axis. Decomposition of the zircon-type phases results in lattice contraction. The oxygen ion transference numbers of $Ce_{1-x}A_xVO_{4+\delta}$ ceramics, determined by the faradaic efficiency measurements in air, are in the range 2×10^{-4} to 6×10^{-3} at 973–1223 K, increasing with temperature. The oxygen ionic conductivity, having activation energy of 87–112 kJ/mol, was found essentially independent of the *A*-site dopant concentration. The ionic transport in $Ce_{0.9}Sr_{0.1}VO_{4+\delta}$ is slightly higher compared to other materials. Contrary to ionic conduction, the *p*-type electronic conductivity and Seebeck coefficient of zircon-type vanadates are determined by the divalent dopant concentration.

Acknowledgments

This research was partially supported by the FCT, Portugal (POCTI program and project BD/6827/2001), and NATO Science for Peace program (project 978002).

References

[1] U.O. Krasovec, B. Orel, R. Reisfeld, Electrochem. Solid State Lett. 1 (1998) 104.
[2] A.M. Salvi, F. Decker, F. Varsano, G. Speranza, Surf. Interface Anal. 31 (2001) 255.
[3] R. Cousin, D. Courcot, E. Abi-Aad, S. Capelle, J.P. Amoureux, M. Dourbin, M. Guelton, A. Aboukais, Colloid. Surf. A 158 (1999) 43.
[4] J. Matta, D. Courcot, E. Abi-Aad, A. Aboukais, Environment and Solar, Proceedings 2000 Mediterranean Conference, IEEE, Piscataway, NJ, 2001, p. 278.
[5] K.V. Narayana, S.K. Masthan, V.V. Rao, P.K. Rao, J. Chem. Res. Synop. 9 (1997) 328.
[6] S. Varma, B.N. Wani, N.M. Gupta, Mater. Res. Bull. 37 (2002) 2117.
[7] E.V. Tsipis, M.V. Patrakeev, V.V. Kharton, N.P. Vyshatko, J.R. Frade, J. Mater. Chem. 12 (2002) 3738.
[8] H.C. Nguyen, J.B. Goodenough, J. Solid State Chem. 119 (1995) 24.
[9] A. Watanabe, J. Solid State Chem. 153 (2000) 174.
[10] W.O. Milligan, L.W. Vernon, J. Phys. Chem. 56 (1952) 145.
[11] B.C. Chakoumakos, M.M. Abraham, L.A. Boatner, J. Solid State Chem. 109 (1994) 197.
[12] R.F. Reidy, K.E. Swider, J. Am. Ceram. Soc. 78 (1995) 1121.
[13] K. Gaur, H.B. Lal, J. Mater. Sci. 20 (1985) 3167.
[14] S.J. Skinner, Solid State Ion. 154–155 (2002) 325.
[15] L.-P. Li, G.-S. Li, Y.-F. Xue, H. Inomata, J. Electrochem. Soc. 148 (2001) J45.
[16] V.V. Kharton, F.M. Figueiredo, L. Navarro, E.N. Naumovich, A.V. Kovalevsky, A.A. Yaremchenko, A.P. Viskup, A. Carneiro, F.M.B. Marques, J.R. Frade, J. Mater. Sci. 36 (2001) 1105.
[17] V.V. Kharton, A.P. Viskup, F.M. Figueiredo, E.N. Naumovich, A.A. Yaremchenko, F.M.B. Marques, Electrochim. Acta 46 (2001) 2879.
[18] V.V. Kharton, A.V. Kovalevsky, A.P. Viskup, F.M. Figueiredo, A.A. Yaremchenko, E.N. Naumovich, F.M.B. Marques, J. Electrochem. Soc. 147 (2000) 2814.
[19] A.V. Kovalevsky, V.V. Kharton, E.N. Naumovich, Inorg. Mater. 32 (1996) 1230.
[20] D.P. Fagg, J.C.C. Abrantes, D. Perez-Coll, P. Nunez, V.V. Kharton, J.R. Frade, Electrochim. Acta 48 (2003) 1023.
[21] J. Rodriguez-Carvajal, Physica B 192 (1993) 55.
[22] M.V. Patrakeev, E.B. Mitberg, A.A. Lakhtin, I.A. Leonidov, V.L. Kozhevnikov, V.V. Kharton, M. Avdeev, F.M.B. Marques, J. Solid State Chem. 167 (2002) 203.
[23] T. Hirata, A. Watanabe, J. Solid State Chem. 158 (2001) 254.
[24] R.D. Shannon, Acta Cryst. A32 (1976) 751.
[25] H. Yokokawa, N. Sakai, T. Kawada, M. Dokiya, J. Am. Ceram. Soc. 73 (1990) 649.
[26] V.V. Kharton, A.A. Yaremchenko, E.N. Naumovich, F.M.B. Marques, J. Solid State Electrochem. 4 (2000) 243.
[27] I.A. Leonidov, A.A. Fotiev, M.Ya. Khodos, Inorg. Mater. 23 (1987) 107.
[28] I.S. Kulikov, Thermodynamics of Oxides, Metallurgia, Moscow, 1986.
[29] P. Schenck, Phase Equilibria Diagrams, CD-RomDatabase, The American Ceramic Society, Westerville, OH, 1998.

[30] V.V. Kharton, E.N. Naumovich, A.A. Vecher, A.V. Nikolaev, J. Solid State Chem. 120 (1995) 128.
[31] V.V. Kharton, A.P. Viskup, A.V. Kovalevsky, E.N. Naumovich, F.M.B. Marques, Solid State Ion. 143 (2001) 337.
[32] A.F. Sammells, R.L. Cook, J.H. White, J.J. Osborne, R.C. MacDuff, Solid State Ion. 52 (1992) 111.
[33] H. Hayashi, H. Inaba, M. Matsuyama, N.G. Lan, M. Dokiya, H. Tagawa, Solid State Ion. 122 (1999) 1.